

RSC Advances



This is an *Accepted Manuscript*, which has been through the Royal Society of Chemistry peer review process and has been accepted for publication.

Accepted Manuscripts are published online shortly after acceptance, before technical editing, formatting and proof reading. Using this free service, authors can make their results available to the community, in citable form, before we publish the edited article. This *Accepted Manuscript* will be replaced by the edited, formatted and paginated article as soon as this is available.

You can find more information about *Accepted Manuscripts* in the [Information for Authors](#).

Please note that technical editing may introduce minor changes to the text and/or graphics, which may alter content. The journal's standard [Terms & Conditions](#) and the [Ethical guidelines](#) still apply. In no event shall the Royal Society of Chemistry be held responsible for any errors or omissions in this *Accepted Manuscript* or any consequences arising from the use of any information it contains.

p-BiOI/n-SnS₂ heterojunction flowerlike structure with enhanced visible-light photocatalytic performance

Tingting Wang^a, Hui Meng^{a*}, Xiang Yu^b, Yizhu Liu^a, Hongbin Chen^b, Yi Zhu^a,
Jinpeng Tang^b, Yexiang Tong^c, Yuanming Zhang^{b*}

a. College of Science and Engineering, Jinan University, Guangzhou 510632, PR China

b. Department of Chemistry, Jinan University, Guangzhou 510632, PR China

c. School of Chemistry & Chemical Engineering, Sun Yat Sen University, Guangzhou 510275, P R China.

Abstract: BiOI/SnS₂ p-n junction is prepared by depositing BiOI particles on flowerlike SnS₂ flakes. The heterojunction formed between p-type BiOI and n-type SnS₂ brings great improved photocatalytic activity compared with pure SnS₂ or BiOI in the degradation of Rhodamine-B dye under visible light and sun-light irradiation. The improved photocatalytic performance is explained by the synergetic effects of the formation of p-n junction between BiOI and SnS₂. The migration of photogenerated carries can be promoted by the electric field established at the heterojunction interfaces, leading to effective separation of the photogenerated electron-hole pairs and reduced electron-hole recombination. The BiOI/SnS₂ heterojunction will find promising applications in photocatalysis and solar energy conversion.

Keywords:

Halogen bismuth oxide; Tin disulfide; Heterojunction; Photocatalysis

*: co-corresponding author

Email: tmh@jnu.edu.cn (Hui Meng) ; tzhangym@jnu.edu.cn (Yuanming Zhang)

1. Introduction

Photocatalysis is a hot topic in solar energy conversion and photo-oxidation of organic pollutants in environmental management¹⁻⁶. Most photocatalysts are semiconductors of oxides and sulfides such as TiO_2 ⁷⁻⁹, ZnO ^{10,11}, SnO_2 ^{12, 13}, Bi_2O_3 ^{14, 15} and CdS ^{16, 17}. However the low energy conversion efficiency limits the application of these materials^{18, 19}. Doping with foreign semiconductor is an effective way to improve the performance of photocatalysts, as the difference between conduction band and valence band of different semiconductors will benefit the separation of photon-generated electron-hole pairs, reduce the recombination and improve the quantum efficiency²⁰⁻²³.

SnS_2 is n-type semiconductor with intriguing optical and electrical properties which makes it an attractive candidate in photocatalysis.²⁴⁻²⁶. However, the band gap (2.18-2.44eV) of SnS_2 (wider compared with the narrow band gap semiconductor such as BiOI) weakens its photocatalytic activity in the visible light region. Various ways have been tried to improve the visible light absorption of SnS_2 ²⁶⁻²⁸. The construction of p-n junction between n-type SnS_2 and p-type narrow band gap semiconductors is an effective way to solve this problem, as the external electric field of p-n junction benefits the separation of electron-hole and enhances the photocatalytic capability dramatically²⁹⁻³¹. In our work BiOI , a p-type semiconductor with a narrow band gap of 1.70-1.83 eV, is chosen as a coupling semiconductor to SnS_2 to achieve high visible light response. The valence band and conduction band potentials of BiOI are more negative than those of SnS_2 , which thermodynamically allows the electrons on the conduction band of BiOI transfers to that of SnS_2 while the holes remain in BiOI ³⁰⁻³⁴. The photogenerated electron-hole pairs will be separated effectively by the p-n junction formed at the p- $\text{BiOI}/\text{n-SnS}_2$ interface^{29,34}, resulting in a reduced electron-hole recombination. Thus, the p- $\text{BiOI}/\text{n-SnS}_2$ heterojunction is expected to possess higher visible-light-driven photocatalytic activity than individual SnS_2 and BiOI . BiOI exhibits the best photocatalytic activity for the degradation of organic pollutants under visible light irradiation among the BiOX (X=Cl, Br, I) family³⁵. To reduce the high recombination probability of electron-hole pairs and improve the slow rate of charge transfer, a lot of composites have been synthesized to

improve the photocatalytic activity of BiOI, such as BiOI/TiO₂³⁶, BiOBr/BiOI³⁷, AgI/BiOI³⁸ and ZnO/BiOI³⁹. A latest work reported a BiPO₄/BiOI composite with excellent enhancement of visible light utilization ability and photocatalytic activity than pure BiOI⁴⁰. But there is no report on the BiOI/SnS₂ composite till now.

In this work, for the first time BiOI was coated on the surface of the flowerlike SnS₂ to form p-BiOI/n-SnS₂ heterojunction. The as-prepared p-n BiOI/SnS₂ junction shows high visible-light photocatalytic activity toward the degradation of RhB in water with high stability. To the best of our knowledge, this is the first report on the preparation of p-BiOI and n-SnS₂ heterojunction with enhanced visible-light photocatalytic performance.

2. Experimental

All the reagents were purchased from Aladdin reagent (China) Co., Ltd and were used as received without further purification. All water was deionized water prepared in lab.

2.1 Synthesis

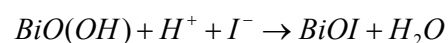
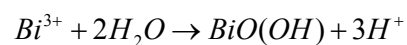
Synthesis of flowerlike SnS₂

In a typical preparation process, 1 mmol SnCl₄·5H₂O, 8.0 mmol thioacetamide and 0.3 g Polyvinyl pyrrolidone (PVP) were dissolved in 40mL deionized water. The mixture was vigorously stirred for 30 min to ensure homogeneous dispersion. The solution was transferred to a 50mL Teflon-lined stainless steel autoclave and maintained at 160°C for 12h. After cooling to room temperature the product was collected by centrifugation, followed by washing thoroughly with deionized water and ethanol. The final product was dried at 60°C in vacuum for 8h.

Synthesis of BiOI/SnS₂

BiOI was coated onto the flowerlike SnS₂ by an impregnating hydroxylation method using BiI₃ as the precursor. In a typical synthesis, 0.94 g of BiI₃ was added into 20 mL ethanol containing 2 drops of 35% HCl. The flowerlike SnS₂ were first immersed in BiI₃ solution for 30 min followed by a slight rinse with ethanol and then dried in an oven at 80°C for 1 h to ensure that BiI₃ was adhered to the surface of SnS₂.

The hydroxylation of BiI₃ is proposed by the following reactions:



2.2 Physical characterizations

The morphologies of the samples were characterized by field emission scanning electron microscopy (FESEM) (JEOL JSM-T300, operated at 10kV) and field emission transmission electronic micrograph (FETEM) (JEOL SM-6330F, operated at 200 kV). Energy dispersive X-ray spectroscopy (EDX) (JEOL JSM-6330F equipped with an X-ray energy dispersive spectrometer) was used to analyze the element composition. The crystal structure of the samples were determined on an X-ray diffractometer (XRD) (MSALXD-2 with Cu-K α radiation), D/Max-III A, Rigaku Co., Japan, CuK1, $\lambda=1.54056$ Å radiation) and selected area electron diffraction (SAED). X-ray photoelectron spectroscopy (XPS) spectra were acquired using an ESCA Lab 250 (Thermo VG) with 200 W Al K α radiation in twin anode and the distance between X-ray gun and sample is about 1 cm. The analysis chamber pressure is about 2×10^{-7} Pa and the pass energy is 20 eV for high resolution scans. The Brunauer–Emmett–Teller (BET) surface areas of the samples were investigated on a TriSTRA 3000 instrument at liquid nitrogen temperature (77.3K). The light absorption ability was analyzed by UV-vis diffuse reflectance spectra (DRS) (Cary 5000) using BaSO₄ as a reference.

2.3 Photocatalytic performance characterizations

Photocatalytic activities of the samples were evaluated by photo-bleaching of Rhodamine B (RhB) under UV-vis (385-740 nm) and visible light ($\lambda>420$ nm) irradiations. Experiments were carried out in a 250 ml cylindrical-shaped-glass reactor at room temperature in the air and at neutral pH conditions. A suspension of 100 mg photocatalyst and 100 ml aqueous solution of RhB (10 mg l⁻¹) was magnetically stirred for at least 2h before irradiation to establish an adsorption-desorption equilibrium. The optical system used for the photocatalytic reaction consisted of a Xenon lamp (XQ350W) and a 420 nm cutoff filter, which was placed under the reaction cell to completely remove all incoming light with wavelengths shorter than 420 nm to ensure irradiation with visible light only. At specific time intervals, 4 ml suspension were sampled and centrifugated at 5000 rpm for 10 minutes to remove the photocatalyst powder. The concentration of remnant RhB in the solution after irradiation was analyzed by UV-vis spectrophotometer by recording the variations of the absorbance band maximum at $\lambda=554$ nm (RhB).

In the cycling test, the most active catalyst was regenerated by centrifugation after the degradation and washed with water for 3-4 times for the complete removal of dye

from the catalysts. Then the catalyst was dried at 60 °C for 8h and reused for another cycle keeping the concentration of dye and photocatalyst unchanged.

2.4 Photoelectrochemical Measurements

In the fabrication of the photo-anode, 20 mg as-prepared photocatalyst powder and 2 ml ethanol solution were mixed homogeneously. The mixture was sprayed on an FTO (fluorine doped tin oxide) glass and allowed to dry under ambient conditions. Photocurrent was measured by an electrochemical workstation (SP-150 from Bio-Logic Science Instruments) in a standard three-electrode system with the as-prepared samples as the working electrodes with an active area of ca. 6 cm², a Pt wire as the counter electrode, and a saturated calomel electrode (SCE) as reference electrode. A 350 W Xe lamp equipped with an ultraviolet cutoff filter ($\lambda > 420$ nm) was utilized as the visible-light source. A 0.1 M Na₂SO₄ aqueous solution was used as the electrolyte.

3. Results and discussion

3.1 Physical characterization of the BiOI/SnS₂ composite

FESEM image (Fig. 1a) shows the flowerlike morphology of the obtained SnS₂ with the average overall diameter of 1-1.5 μ m. A high-magnified picture in Fig. 1b shows that the SnS₂ flower is comprised by several self-assembled irregular plates in the similar way like the petals connected with each other to form a Rieger begonia (inset of Fig. 1b). Fig. 1c and d are SEM images of the flowerlike SnS₂ with BiOI deposited on the surface. SnS₂ keeps its structure after the deposition, the flakes of the SnS₂ flower are covered by BiOI particles with the diameter of 5-40 nm.

It is proposed that the surfactant (PVP) present in the solution plays a key role in the assembly of SnS₂ flakes into the flower structure. In the crystal growth process the surface of the crystal is covered by PVP molecules, the Van der Waals force and hydrogen bond play crucial role in the formation of the flowerlike structure. The formation of flowerlike morphology is based on heterogeneous nucleation. SnS₂ nanoparticles are formed during the initial stage of the hydrothermal process, PVP molecules stabilize the particles and prevent the aggregation of the particles. After a heterogeneous nucleation process the particles grow along the specific energetically favorable sites that are likely to be promoted by the surfactant molecules into the flowerlike structure⁴¹.

The microstructure of SnS₂ was further characterized by means of TEM and HRTEM. As shown in Fig. 2a and b, the SnS₂ flowers were decomposed into flakes after the ultrasonic treatment in the sample preparation for TEM observation. The morphology was the same with that observed in FESEM images (Fig. 1a and b). The lattice fringe was observed by HRTEM of a selected area of a single flake as shown in Fig. 2c. The distance between the lattice fringes is 0.278 nm, corresponding to the d-spacing of (011) lattice planes of hexagonal phase SnS₂. The SAED in Fig.2d shows hexagonal array of spots, which revealed the single crystal structure of the flake. The d value of the (011) facet from the SAED is in accordance with that from HRTEM. From SAED it is concluded that the [001] orientation is the preponderant growth direction of the SnS₂ flake, which is parallel to the (011) facet.

TEM verifies the formation of BiOI/SnS₂ p-n junction. The size and morphology of both BiOI and SnS₂ in the TEM images of Fig.3a and b are in consistent with the SEM images in Fig.1c. Fig.3b is an enlarged picture of the BiOI/SnS₂ heterojunction, from which it is observed that the deposited particles disperse uniformly throughout the surface of the SnS₂ flake and the particle size is 5-20 nm. In TEM the big particles of 40nm in SEM are not found, this may be caused by the ultrasonic treatment in the TEM sample preparation, only leaving small particles on the surface. The crystal property of the BiOI/SnS₂ heterojunction is studied by HRTEM as shown in Fig.3c. Two d values of lattice spacing are indexed to be 0.278 and 0.301 nm, corresponding to the spacing of the (011) plane of SnS₂ and (012) plane of BiOI, respectively. The (011) peak of SnS₂ and (012) peak of BiOI are the strongest peak presented in the XRD of Fig.4a and b, which indicates the presence of the mixed phase of SnS₂ and BiOI in the flowerlike composite. The SAED pattern (Fig. 3d) indexed out the diffraction patterns of (012), (110) and (122) planes of BiOI. The (012) plane is also observed in the HRTEM in Fig.3c and the (110) plane is parallel to the growth direction of BiOI. The (011), (102) and (022) facets of SnS₂ are also indexed.

Energy dispersive X-ray spectroscopy (EDS) mapping were conducted to study the detailed information about the elemental dispersion of Sn, S, Bi, O and I elements in the BiOI/SnS₂ composite (Fig. 4). Fig. 4b and c proved the main composition of the flake is SnS₂ since Sn and S are predominant elements throughout the flake. It should be noted that Bi, O and I elements are randomly distributed throughout the SnS₂ flake and the density of these three elements is not so high as Sn and S, this is because BiOI exist in particles on the surface of SnS₂ flakes, which is in accordance with the

morphology information from the SEM and TEM results.

XRD is used to study the crystal composition of the BiOI/SnS₂ composite. Fig.5 shows the XRD patterns of the as-synthesized pure SnS₂, BiOI and BiOI/SnS₂ composites. From Fig.5 a and b hexagonal SnS₂ phase and tetragonal BiOI phase are identified from standard card JCPDS 89-2028 and JCPDS 73-2062, respectively. BiOI/SnS₂ composites are composed by tetragonal BiOI phase and hexagonal SnS₂ phase, which is proved by the coexistence of all characteristic peaks of both SnS₂ and BiOI phases (Fig. 5c). It is found the full width at half maximum (FWHM) of the BiOI peaks in Fig.5c is much wider than that of Fig.5b, this is a sign of smaller crystal size of BiOI in the BiOI/SnS₂ composites than pure BiOI.

The chemical state and valence band states of the elements on the surface of the BiOI/SnS₂ composite are studied with the X-ray photoelectron spectroscopy (XPS). In this work, XPS results can also provide useful information on the structure of the material and help to explain the enhanced photocatalytic performance. XPS spectrum in Fig.6a disclosed the presence of Bi, O, I, Sn and S elements. The result is in accordance with the XRD and EDS results. Typical high-resolution XPS spectra of Sn 3d and Bi 4f are shown in Fig. 6b and 6d. It is clear that the binding energies of Sn 3d_{5/2} (486.4 eV) and Sn 3d_{3/2} (494.9 eV) in BiOI/SnS₂ composites are higher than those of pure SnS₂ (487.1 eV and 493.4 eV), which is characteristic of Sn⁴⁺^{34,42,43}. At the same time the binding energies of Bi 4f_{7/2} and Bi 4f_{5/2} peaks of SnS₂/BiOI are located at 159.0 eV and 164.3 eV which are lower than those of pure BiOI (159.4 eV and 164.3 eV), which is characteristic of Bi³⁺³⁰⁻³². This is explained by the fact that the conduction band edge of BiOI is lower than that of SnS₂, and the Fermi level of BiOI is lower than that of SnS₂, so that the electrons on Sn atom can transfer to the Bi atom in BiOI dispersed on the surface of SnS₂, which changes the outer electron cloud density of Sn and Bi and makes the binding energies of Sn 3d_{5/2} and Sn 3d_{3/2} increase and that of Bi 4f_{7/2} and Bi 4f_{5/2} decrease^{33, 34}. The interaction of the Fermi level electron and electron cloud may change the property of individual SnS₂ and BiOI, leading to new properties. Two peaks at 161.4 eV and 162.5 eV shown in Fig. 6c are attributed to S 2p_{3/2} and S 2p_{1/2}, which are characteristic of S²⁻ in SnS₂^{34,42,43}. Fig. 6e shows the high-resolution XPS spectrum of O 1s, which can be fitted into two peaks. The main peak at 530.9 eV belongs to the Bi-O bonds in (BiO)₂²⁺ an BiOI, and the

peak at 532.2 eV is assigned to the hydroxyl groups on the surface³⁰⁻³². As to the high-resolution spectra of the I 3d (Fig. 6f), two peaks at 619.1 and 630.3 eV attributed to I 3d_{5/2} and I 3d_{3/2} respectively, can be ascribed to I⁻ in BiOI and BiOI/SnS₂ composites³⁰⁻³². In conclusion, according to the XPS results, the coexistence of SnS₂ and BiOI in the composites is confirmed and the formation of a p-n junction caused the interaction of the Fermi level electron and electron cloud of SnS₂ and BiOI.

The specific BET surface areas (S_{BET}) and pore structure of the prepared samples were investigated using nitrogen adsorption-desorption measurements, the results are in the supporting information. Fig. S1 shows the nitrogen adsorption-desorption isotherms of the samples. According to the Brunauer-Emmett-Teller (BDDT) classification, the isotherms and the shapes of hysteresis loops in Fig. S1 are types IV and H3, indicating the pore-size distributions in the mesoporous regions, which is associated with mesopores formed due to deposition of BiOI particles. As shown in Table 1, the S_{BET} of the BiOI/SnS₂ composite is 24.75 m²/g, which is sixfold larger in comparison to pure SnS₂ (4.09 m²/g). Considering the fact that the morphology of the SnS₂ remains almost unchanged after the formation of BiOI/SnS₂ composite (SEM in Fig. 1), the increased S_{BET} of the BiOI/SnS₂ composite compared with pure SnS₂ can only be ascribed to the BiOI particles on the surface of the SnS₂ flakes. Moreover, the SnS₂/BiOI composites also demonstrate nearly 6 times greater pore volume of 0.1475 cm³/g, compared to pure SnS₂ (0.0255 cm³/g). Insert in Fig. S1 is the pore-size distribution (PSD). The PSD curve of pure SnS₂ is unimodal with mesopore value of 7.4 nm. The PSD curve of SnS₂/BiOI composite is tri-modal with the value of 2.2 nm, 4.6 nm and 29 nm. These results prove that BiOI coatings on SnS₂ result in a greater surface area and pore volume, which can benefit the availability of more surface active sites and facilitate mass transfer of the reactants. The larger S_{BET} and pore volume is an important factor leading to an enhanced photocatalytic activity.

3.2 Photocatalytic characterization of the BiOI/SnS₂ composite

The optical absorption properties of the unmodified SnS₂, BiOI and BiOI/SnS₂ are characterized by UV-vis diffuse reflectance spectroscopy. Fig. 7a shows that pure SnS₂

primarily absorbs the ultraviolet light with wavelength below 400 nm, which is determined by the intrinsic band gap of SnS₂. In contrast, BiOI and BiOI/SnS₂ exhibit an obvious red shift and show strong absorptions in the wavelength ranging from 400 to 650 nm. This indicates that the incorporation of BiOI can effectively extend the light absorption edge of SnS₂ from ultraviolet into visible region. Based on the theory of optical absorption for direct band gap semiconductors, the band gap energy (E_g) of the samples are calculated according to the following equation^{17,44}:

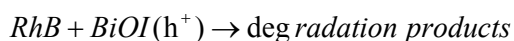
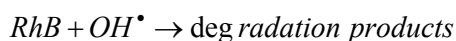
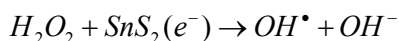
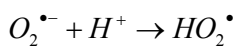
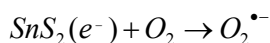
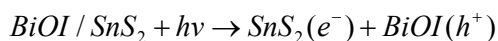
$$\alpha h\nu = A(h\nu - E_g)^{1/2}$$

where α , h , ν , E_g , A are the absorption coefficient, Planck constant, light frequency, band gap energy, and a constant, respectively^{44,45}. By extrapolating the linear portion of $(\alpha h\nu)^2$ vs. $(h\nu)$ curves (Fig. 7b), the E_g of SnS₂, BiOI and BiOI/SnS₂ are estimated to be about 2.45, 1.82, 2.02eV, respectively. The E_g value of BiOI/SnS₂ is between those of pure SnS₂ and BiOI, this proves the formation of the BiOI/SnS₂ p-n junction. The conduction band (CB) of SnS₂ and valence band (VB) of BiOI can be determined by the photoelectrochemical method. In heterojunction the flow direction of electrons depends on their relative band edge positions. The photocurrent spectra of SnS₂ and BiOI are shown in Fig. S2. In the photocurrent spectra, the flat band potential of SnS₂ is observed at -0.96 V versus SCE. For n-type semiconductor, the flat band potential is closely related to the bottom of the CB. According to the measured E_g value of SnS₂ (2.45 eV), the VB is calculated to be 1.50 eV^{26,33}. The photocurrent onset potential of BiOI gives the value VB edge of +0.53 V versus SCE. The band gap energy of BiOI is 1.82 eV, the CB minimum is calculated to be -1.29 eV^{33,45}. Scheme 1 shows the energy band edge positions from above calculations. Before contact the conduction band edge and Fermi level of BiOI are lower than those of SnS₂. After contact when a p-n junction is formed, the charge carriers transfer from BiOI to SnS₂ to form an external electric field at the heterojunction interface³⁰⁻³³. The Fermi levels of n-SnS₂ and p-BiOI are aligned under thermal equilibrium conditions, and the external electric field is directed from n-SnS₂ to p-BiOI, thus preventing the charge migrating from n-SnS₂ into p-BiOI. Meanwhile, the energy band positions of SnS₂ in

BiOI/SnS₂ heterojunction are shifted toward the downward direction and that p-BiOI in BiOI/SnS₂ heterojunction toward the upward direction along with the Fermi level^{32, 33, 46}. Therefore, the band positions of BiOI and SnS₂ in the heterojunction have a type-II band structure, which means the CB and VB of BiOI lie above those of SnS₂^{29, 33}. BiOI absorbs photons of energy greater than the band gap energy under visible-light irradiation, exciting the electrons in the VB to the CB and leaving holes in BiOI. The electrons in the conduction band of the p-type BiOI then transfer to the n-type SnS₂, and the holes remain in the valence band of BiOI. The migration of photogenerated carriers can be promoted by the inner electric field established at the heterojunction interfaces^{30-33, 46}. Thus, the photogenerated electron-hole pairs will be effectively separated due to the formation of a junction between the p-BiOI and n-SnS₂ interface, resulting in a reduced electron-hole recombination.

The photocatalytic activity of BiOI/SnS₂ heterojunction was evaluated by the degradation of RhB, a typical organic contaminant. Fig. 8 presents the changement of RhB concentration (C/C^0) with irradiation time at wavelengths in the range of 385-740 nm and visible light irradiations at $\lambda > 420$ nm, respectively. For comparison, the photocatalytic activity of Degussa's P₂₅ and the degradation of RhB without photocatalysts were tested under the same conditions. The blank test without photocatalysts shows that RhB is very stable and does not decompose even after long-time illumination with UV-vis or visible light irradiations. A rapid decrease in the concentration of RhB with time is realized in the presence of the as-prepared BiOI/SnS₂ heterojunction photocatalyst. For comparison, the photocatalytic property of pure SnS₂ and BiOI were also tested. All the samples exhibited much higher photocatalytic activity under UV-vis and visible light irradiation compared to the standard (Degussa's P₂₅). Among them BiOI/SnS₂ heterojunction showed the highest RhB removal rate with total decomposition within only 30 min under UV-vis light irradiation and within only 50 min under visible light irradiation, which is 6.6 times and 5.3 times higher than that of the standard (Degussa's P₂₅). After 50 minutes of visible irradiation the degradation efficiency of RhB on pure SnS₂ is less than 38%, which is significantly less than that of BiOI/SnS₂ heterojunction.

The degradation of RhB by the BiOI/SnS₂ heterojunction may involve the following steps: under illumination, CB electrons (e⁻) will accumulate on the surface of SnS₂ and holes (h⁺) on BiOI. Super oxide radicals (O₂^{•-}) are then formed by the combination of electrons (e⁻) and oxygen on the surface of the catalyst, which again react with protons and photogenerated electrons to form hydroxyl radical species (OH[•]). Finally some highly active species, i.e., superoxide radicals, hydroxyl radicals, hydroxyl radicals are formed, together with holes on BiOI, these species are responsible for the degradation of organic pollutants. The details are presented in below reactions:



The remarkable improvement of the photocatalytic performance of BiOI/SnS₂ heterojunction is explained by the following two reasons: (i) the photo absorption range of SnS₂ is extended to the visible region by the composition with BiOI due to the sensitization of BiOI. (ii) The p-n junction formed between the p-type BiOI and n-type SnS₂ helps in separating electron-hole pairs at the interface. The separated electrons and holes are then free to initiate the degradation reaction of RhB dye adsorbed on the surfaces of photocatalyst with enhanced photocatalytic activity.

The regeneration and stability of the photocatalyst are the two major factors to be considered in practical applications. The results for the recycling performance of the BiOI/SnS₂ heterojunction are shown in Fig. 9. It is obvious that photocatalytic efficiency does not exhibit significant loss after ten recycles, indicating that the

BiOI/SnS₂ heterojunction displays high stability and do not suffer from photocorrosion during the photocatalytic degradation of RhB.

To further investigate the photocatalytic mechanism, the transient photocurrent responses of the samples were recorded via several irradiation on-off cycles. The representative plots are shown in Fig. 10. When the light was turned on the photocurrent reached a high point and followed by a fast decline, forming a spike, then decreased gradually until a constant value. The photocurrent was instantaneously close to zero as long as the light was switched off. The initial anodic photocurrent spike is caused by the separation of electron-hole pairs at the BiOI/SnS₂ p-n junction interface^{32, 47}. Holes move to the BiOI surface, where they are trapped or captured by reduced species in the electrolyte. At the same time the electrons are transported to the conduction band of SnS₂. The decay of the photocurrent is caused by the recombination of photogenerated electron-hole pairs. Instead of capturing electrons from the electrolyte, a portion of the holes at the surface of BiOI recombine with electrons from the conduction band of SnS₂ or just accumulate at the surface^{32,39,47}. The electrons in the conduction band of SnS₂ take part in the reduction of the photogenerated oxidized species in the electrolyte, which results in the decay of the photocurrent. When the separation and recombination of the electron-hole pairs reach an equilibration, a constant current is reached. When the light is turned off, the holes accumulated at the BiOI surface and the electrons in SnS₂ conduction band are recombined simultaneously, leading to a fast drop of the photocurrent to zero. It can be seen from Fig.10 that BiOI/SnS₂ p-n junction exhibits a prompt generation of photocurrent with good reproducibility. This is because the p-n junction facilitates the separation of electron-hole pairs by the external electrostatic field at the heterojunction interface, which is the origin of the synergetic effect resulting in the high photocatalytic performance of the BiOI/SnS₂ p-n junction.

Conclusions:

In summary, a novel p-BiOI/n-SnS₂ heterojunction was synthesized by coating BiOI on the flowerlike SnS₂. The formation of BiOI/SnS₂ heterojunctions was confirmed by XRD, TEM and XPS. The wide band gap of SnS₂ was effectively sensitized in the visible region, which is confirmed by UV-vis DRS. The p-n junction greatly improves the separation of the photogenerated charge carriers, which is proved by the transient photocurrent response experiments. A dramatic enhancement in the visible light

photocatalytic performance of BiOI/SnS₂ heterojunction is observed, which is explained by the synergetic effects of several factors including the strong visible absorption, the formation of p-n junction, and the formation of an external electrostatic field. The easy synthesis and high degradation efficiency under UV and visible light makes the novel photocatalyst a very promising candidate for application in the degradation of organic pollutants.

Acknowledgements:

This work was supported by National Natural Science Foundation of China (21276104, 21106190, 21476096), Program of the Pearl River Young Talents of Science and Technology in Guangzhou (2013J2200040).

References

- (1) Maeda, K.; Teramura, K.; Lu, D.; Takata, T.; Saito, N.; Inoue, Y.; Domen, K. Photocatalyst Releasing Hydrogen from Water. *Nature* 2006, 440, 295-295.
- (2) Khan, S. U. M.; Al-Shahry, M.; Ingler, W. B. Efficient Photochemical Water Splitting by a Chemically Modified n-TiO₂. *Science* 2002, 297, 2243-2245.
- (3) Zhang, J. S.; Sun, J. H.; Maeda, K.; Domen, K.; Liu, P.; Antonietti, M.; Fu, X. Z.; Wang, X. C. Sulfur-Mediated Synthesis of Carbon Nitride: Band-gap Engineering and Improved Functions for Photocatalysis. *Energy Environ. Sci.* 2011, 4, 675–678.
- (4) Maeda, K.; Xiong, A.; Yoshinaga, T.; Ikeda, T.; Sakamoto, N.; Hisatomi, T.; Takashima, M.; Lu, D.; Kanehara, M.; Setoyama, T. Photocatalytic Overall Water Splitting Promoted by Two Different Cocatalysts for Hydrogen and Oxygen Evolution under Visible Light. *Angew. Chem.* 2010, 122, 4190-4193.
- (5) Pan, C.; Xu, J.; Wang, Y.; Li, D.; Zhu, Y. Dramatic Activity of C₃N₄/BiPO₄ Photocatalyst with Core/Shell Structure Formed by Self-Assembly. *Adv. Funct. Mater.* 2012, 22, 1518-1524.
- (6) Zhou, W.; Yin, Z.; Du, Y.; Huang, X.; Zeng, Z.; Fan, Z.; Liu, H.; Wang, J.; Zhang, H. Synthesis of Few-Layer MoS₂ Nanosheet-Coated TiO₂ Nanobelt Heterostructures for Enhanced Photocatalytic Activities. *Small* 2013, 9, 140-147.

- (7) Chuangchote, S.; Jitputti, J.; Sagawa, T.; Yoshikawa, S. Photocatalytic Activity for Hydrogen Evolution of Electrospun TiO₂ Nanofibers. *ACS Appl. Mater. Interfaces* 2009, 1, 1140-1143.
- (8) Liu, S.; Yu, J.; Jaroniec, M. Tunable Photocatalytic Selectivity of Hollow TiO₂ Microspheres Composed of Anatase Polyhedra with Exposed {001} Facets. *J. Am. Chem. Soc.* 2010, 132, 11914-11916.
- (9) Tan, L. K.; Kumar, M. K.; An, W. W.; Gao, H. Transparent, Well-Aligned TiO₂ Nanotube Arrays with Controllable Dimensions on Glass Substrates for Photocatalytic Applications. *ACS Appl. Mater. Interfaces* 2010, 2, 498-503.
- (10) Wang, J.; Wang, Z.; Huang, B.; Ma, Y.; Liu, Y.; Qin, X.; Zhang, X.; Dai, Y. Oxygen Vacancy Induced Band-Gap Narrowing and Enhanced Visible Light Photocatalytic Activity of ZnO. *ACS Appl. Mater. Interfaces* 2012, 4, 4024-4030.
- (11) Mu, J.; Shao, C.; Guo, Z.; Zhang, Z.; Zhang, M.; Zhang, P.; Chen, B.; Liu, Y. High Photocatalytic Activity of ZnO– Carbon Nanofiber Heteroarchitectures. *ACS Appl. Mater. Interfaces* 2011, 3, 590-596.
- (12) Zhang, Y. C.; Du, Z. N.; Li, K. W.; Zhang, M.; Dionysiou, D. D. High-performance Visible-Light-Driven SnS₂/SnO₂ Nanocomposite Photocatalyst Prepared via In Situ Hydrothermal Oxidation of SnS₂ Nanoparticles. *ACS Appl. Mater. Interfaces* 2011, 3, 1528-1537.
- (13) Sinha, A. K.; Pradhan, M.; Sarkar, S.; Pal, T. Large-Scale Solid-State Synthesis of Sn-SnO₂ Nanoparticles from Layered SnO by Sunlight: a Material for Dye Degradation in Water by Photocatalytic Reaction. *Environ. Sci. Technol.* 2013, 47, 2339-2345.
- (14) Jiang, H. Y.; Liu, J.; Cheng, K.; Sun, W.; Lin, J. Enhanced Visible Light Photocatalysis of Bi₂O₃ upon Fluorination. *J. Phys. Chem. C* 2013, 117,

20029-20036.

(15) Fan, H.; Li, H.; Liu, B.; Lu, Y.; Xie, T. Photoinduced Charge Transfer Properties and Photocatalytic Activity in Bi₂O₃/BaTiO₃ Composite Photocatalyst. *ACS Appl. Mater. Interfaces* 2012, 4, 4853-4857.

(16) Shi, Y.; Li, H.; Wang, L.; Shen, W.; Chen, H. Novel α -Fe₂O₃/CdS cornlike nanorods with enhanced photocatalytic performance. *ACS Appl. Mater. Interfaces* 2012, 4, 4800-4806.

(17) Luo, M.; Liu, Y.; Hu, J.; Liu, H.; Li, J. One-Pot Synthesis of CdS and Ni-Doped CdS Hollow Spheres with Enhanced Photocatalytic Activity and Durability. *ACS Appl. Mater. Interfaces* 2012, 4, 1813-1821.

(18) Etacheri, V.; Seery, M. K.; Hinder, S. J.; Pillai, S. C. Oxygen Rich Titania: A Dopant Free, High Temperature Stable, and Visible-Light Active Anatase Photocatalyst. *Adv. Funct. Mater.*, 2011, 21, 3744-3752.

(19) Roy, N.; Sohn, Y.; Pradhan, D. Synergy of Low-energy {101} and High-Energy {001} TiO₂ Crystal Facets for Enhanced Photocatalysis. *ACS nano* 2013, 7, 2532-2540.

(20) Asahi, R.; Morikawa, T.; Ohwaki, T.; Aoki, K.; Taga, Y. Visible-Light Photocatalysis in Nitrogen-Doped Titanium Oxides. *Science* 2001, 293, 269-271.

(21) Wang, M.; Iocozzia, J.; Sun, L.; Lin, C.; Lin, Z. Semiconductor TiO₂ Nanotube Arrays for Photocatalysis. *Energy Environ. Sci.* 2014, 7, 2182-2202.

(22) Mu, Q.; Zhang, Q.; Wang, H.; Li, Y. Facile Growth of Vertically Aligned BiOCl Nanosheet Arrays on Conductive Glass Substrate with High Photocatalytic Properties. *J. Mater. Chem.* 2012, 22, 16851-16857.

(23) Wang, C.; Guo, Y.; Yang, Y.; Chu, S.; Zhou, C.; Wang, Y.; Zou, Z. Sulfur-Doped Polyimide Photocatalyst with Enhanced Photocatalytic Activity under Visible Light

Irradiation. *ACS Appl. Mater. Interfaces* 2014, 6, 4321-4328.

(24) Wei, R.; Hu, J.; Zhou, T.; Zhou, X.; Liu, J.; Li, J. Ultrathin SnS₂ Nanosheets with Exposed {001} Facets and Enhanced Photocatalytic Properties. *Acta Mater.* 2014, 66, 163-171.

(25) Zhang, Y. C.; Li, J.; Zhang, M.; Dionysiou, D. D. Size-Tunable Hydrothermal Synthesis of SnS₂ Nanocrystals with High Performance in Visible Light-Driven Photocatalytic Reduction of Aqueous Cr (VI). *Environ. Sci. Technol.* 2011, 45, 9324-9331.

(26) Hu, X.; Song, G.; Li, W.; Peng, Y.; Jiang, L.; Xue, Y. F.; Liu, Q.; Chen, Z. G.; Hu, J. Q. Phase-Controlled Synthesis and Photocatalytic Properties of SnS, SnS₂ and SnS/SnS₂ Heterostructure Nanocrystals. *Mater. Res. Bull.* 2013, 48, 2325-2332.

(27) Zhang, Z. Y.; Shao, C. L.; Li, X. H.; Sun, Y. Y.; Zhang, M. Y.; Mu, J. B.; Zhang, P.; Guo, Z. C.; Liu, Y. C. Hierarchical Assembly of Ultrathin Hexagonal SnS₂ Nanosheets onto Electrospun TiO₂ Nanofibers: Enhanced Photocatalytic Activity Based on Photoinduced Interfacial Charge Transfer. *Nanoscale* 2013, 5, 606-618.

(28) An, X.; Jimmy, C. Y.; Tang, J. Biomolecule-Assisted Fabrication of Copper Doped SnS₂ Nanosheet-Reduced Graphene Oxide Junctions with Enhanced Visible-Light Photocatalytic Activity. *J. Mater. Chem. A* 2014, 2, 1000-1005.

(29) Wang, Y. J.; Wang, Q. S.; Zhan, X. Y.; Wang, F. M.; Safdar, M.; He, J. Visible Light Driven Type II Heterostructures and Their Enhanced Photocatalysis Properties: a Review. *Nanoscale* 2013, 5, 8326-8339.

(30) Jiang, D. L.; Chen, L. L.; Zhu, J. J.; Chen, M.; Shi, W. D.; Xie, J. M. Novel P-N Heterojunction Photocatalyst Constructed by Porous Graphite-Like C₃N₄ and Nanostructured BiOI: Facile Synthesis and Enhanced Photocatalytic Activity. *Dalton Trans.* 2013, 42, 15726-15734.

- (31) Hou, D.; Hu, X.; Hu, P.; Zhang, W.; Zhang, M.; Huang, Y. Bi₄Ti₃O₁₂ Nanofibers–BiOI Nanosheets P-N Junction: Facile Synthesis and Enhanced Visible-Light Photocatalytic Activity. *Nanoscale* 2013, 5, 9764-9772.
- (32) Dai, G.; Yu, J.; Liu, G. Synthesis and Enhanced Visible-Light Photoelectrocatalytic Activity of P-N Junction BiOI/TiO₂ Nanotube Arrays. *J. Phys. Chem. C* 2011, 115, 7339-7346.
- (33) Reddy, K. H.; Martha, S.; Parida, K. M. Fabrication of Novel P-BiOI/N-ZnTiO₃ Heterojunction for Degradation of Rhodamine 6G under Visible Light Irradiation. *Inorg. Chem.* 2013, 52, 6390-6401.
- (34) Yang, F.; Han, G.; Fu, D.; Chang, Y.; Wang, H. Improved Photodegradation Activity of TiO₂ via Decoration with SnS₂ Nanoparticles. *Mater. Chem. Phys.* 2013, 140, 398-404.
- (35) Zhang, X. Z.; Ai, H.; Jia, F. L.; Zhang, L. Z. Generalized one-pot synthesis, characterization, and photocatalytic activity of hierarchical BiOX (X = Cl, Br, I) nanoplate microspheres, *J. Phys. Chem. C*, 2008, 112, 747-753.
- (36) Zhang, X.; Zhang, L.Z.; Xie, T. F.; Wang, D. J. Low-Temperature Synthesis and High Visible-Light-Induced Photocatalytic Activity of BiOI/TiO₂ Heterostructures, *J. Phys. Chem. C*, 2009, 113, 7371-7378.
- (37) Cao, J.; Xu, B. Y.; Lin, H. L.; Luo, B.D.; Chen, S.F. Chemical etching preparation of BiOI/BiOBr heterostructures with enhanced photocatalytic properties for organic dye removal, *Chem. Eng. J.*, 2012, 91-99.
- (38) Cheng, H. F.; Wang, W. J.; Huang, B. B.; Wang, Z. Y.; Zhan, J.; Qin, X. Y.; Zhang, X. Y.; Dai, Y. Tailoring AgI nanoparticles for the assembly of AgI/BiOI hierarchical hybrids with size-dependent photocatalytic activities, *J. Mater. Chem. A*, 2013, 1, 7131-7136.

- (39) Jiang, J.; Zhang, X.; Sun, P. B.; Zhang, L.Z. ZnO/BiOI Heterostructures: Photoinduced Charge-Transfer Property and Enhanced Visible-Light Photocatalytic Activity, *J. Phys. Chem. C*, 2011, 115, 20555-20564.
- (40) Liu, Y. F.; Yao, W. Q.; Li, D.; Zong, R. L.; Zhang, M.; Ma, X. G.; Zhu, Y. F. Enhancement of visible light mineralization ability and photocatalytic activity of BiPO₄/BiOI, *Appl. Catal. B: Environ.* 2015, 163, 547-553.
- (41) Ota, J.; Roy, P.; Srivastava, S. K.; Nayak, B. B.; Saxena, A. K. Morphology Evolution of Sb₂S₃ under Hydrothermal Conditions: Flowerlike Structure to Nanorods, *Cryst. Growth Des.* 2008, 8, 2019-2023.
- (42) Wang, J.; Li, X.; Li, X.; Zhu, J.; Li, H. Mesoporous Yolk-Shell SnS₂-TiO₂ Visible Photocatalysts with Enhanced Activity and Durability in Cr (vi) Reduction. *Nanoscale* 2013, 5, 1876-1881.
- (43) Lei, Y.; Song, S.; Fan, W.; Xing, Y.; H. Zhang, J. Facile Synthesis and Assemblies of Flowerlike SnS₂ and In³⁺-Doped SnS₂: Hierarchical Structures and Their Enhanced Photocatalytic Property. *J. Phys. Chem. C* 2009, 113, 1280-1285.
- (44) Shang, M.; Wang, W.; Zhang, L. Preparation of BiOBr Lamellar Structure with High Photocatalytic Activity by CTAB as Br Source and Template. *J. Hazard. Mater.* 2009, 167, 803-809.
- (45) Xiao, X.; Zhang, W. D. Facile Synthesis of Nanostructured BiOI Microspheres with High Visible Light-Induced Photocatalytic Activity. *J. Mater. Chem.* 2010, 20, 5866-5870.
- (46) Chen, L.; Yin, S. F.; Luo, S. L.; Huang, R.; Zhang, Q.; Hong, T.; Peter, C. T. Bi₂O₂CO₃/BiOI Photocatalysts with Heterojunctions Highly Efficient for Visible-Light Treatment of Dye-Containing Wastewater. *Ind. Eng. Chem. Res.* 2012, 51, 6760-6768.
- (47) Yu, J.; Dai, G.; Huang, B. Fabrication and Characterization of Visible-Light-Driven Plasmonic Photocatalyst Ag/AgCl/TiO₂ Nanotube Arrays. *J. Phys. Chem. C* 2009, 113, 16394-16401.

Table 1

Specific BET surface areas, pore parameters for the as-synthesized samples.

Samples	S_{BET} (m^2/g)	Total volume (cm^3/g)	Peak pore diameter (nm)
SnS_2	4.09	0.0255	2.2 / 4.6 / 29
SnS_2/BiOI	24.75	0.1475	7.4

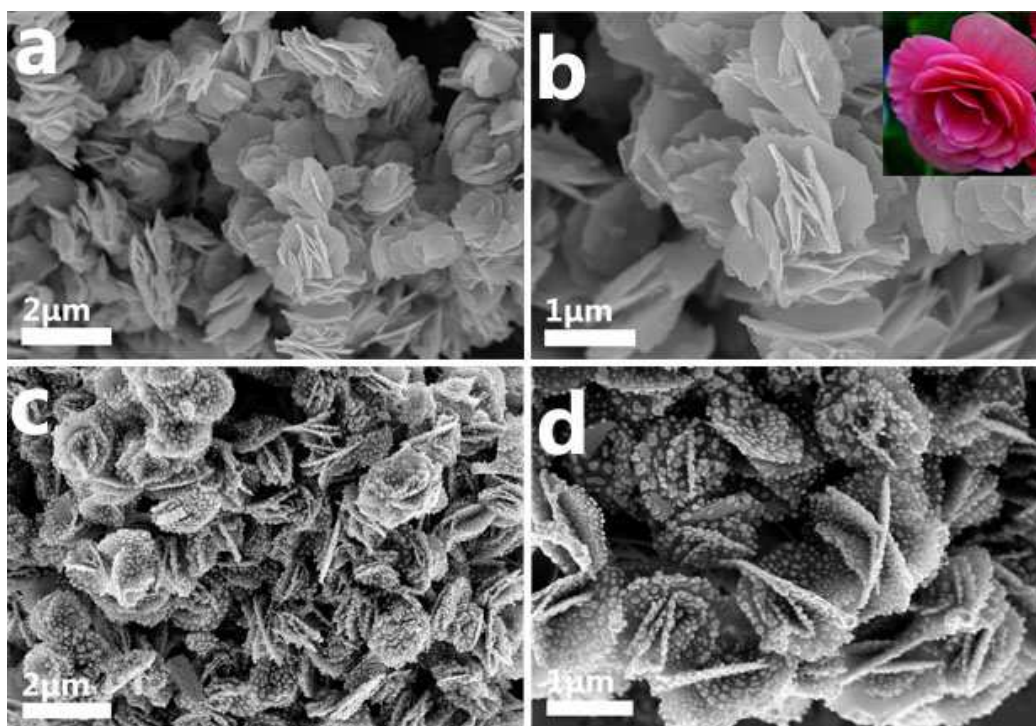


Fig. 1 FESEM images of self-organized SnS₂ (a, b) and BiOI/SnS₂ (c, d). The inset picture in b is the picture of a Rieger begonia for illustrating.

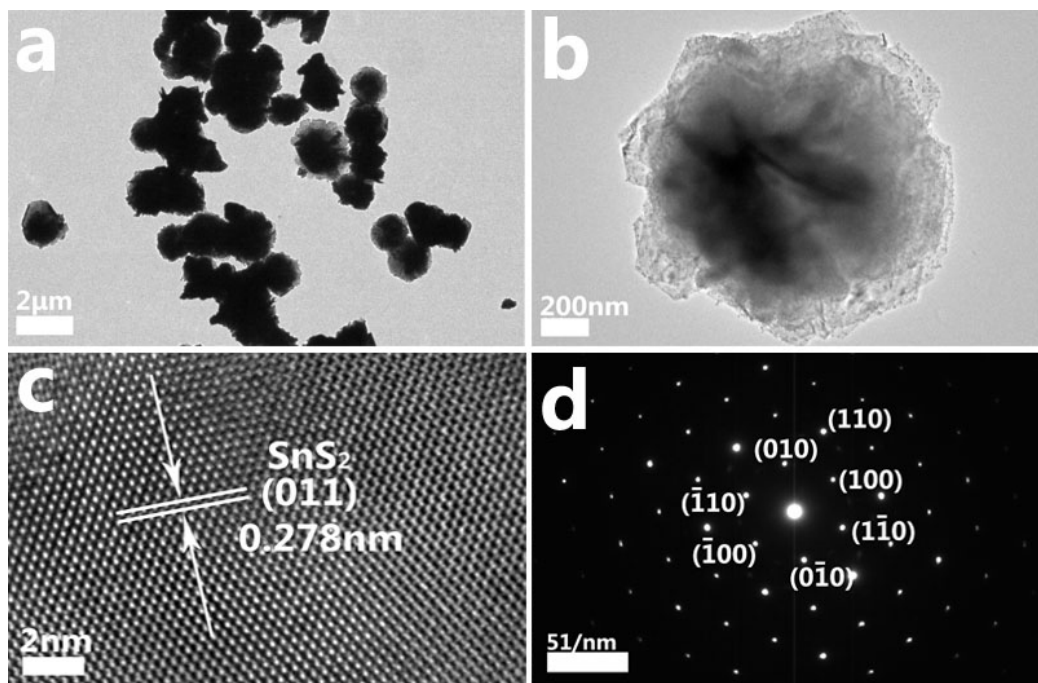


Fig. 2 FETEM images (a, b and c) and SEAD pattern (d) of as prepared SnS₂.

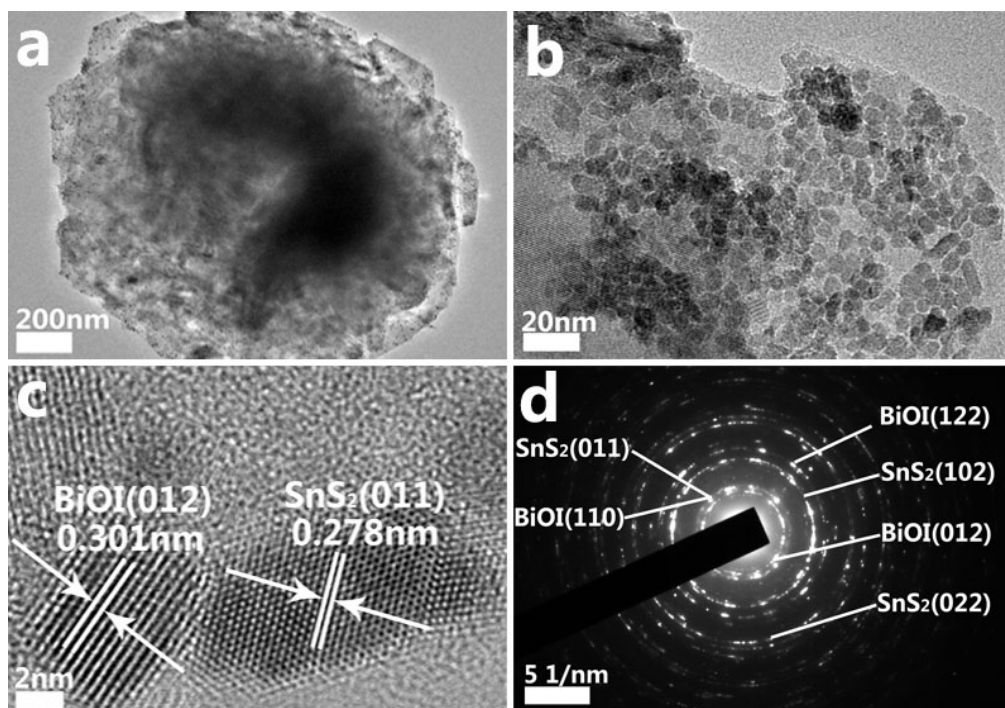


Fig. 3 FETEM images (a, b and c) and SEAD pattern (d) of as prepared BiOI/SnS₂ flowerlike heterojunction.

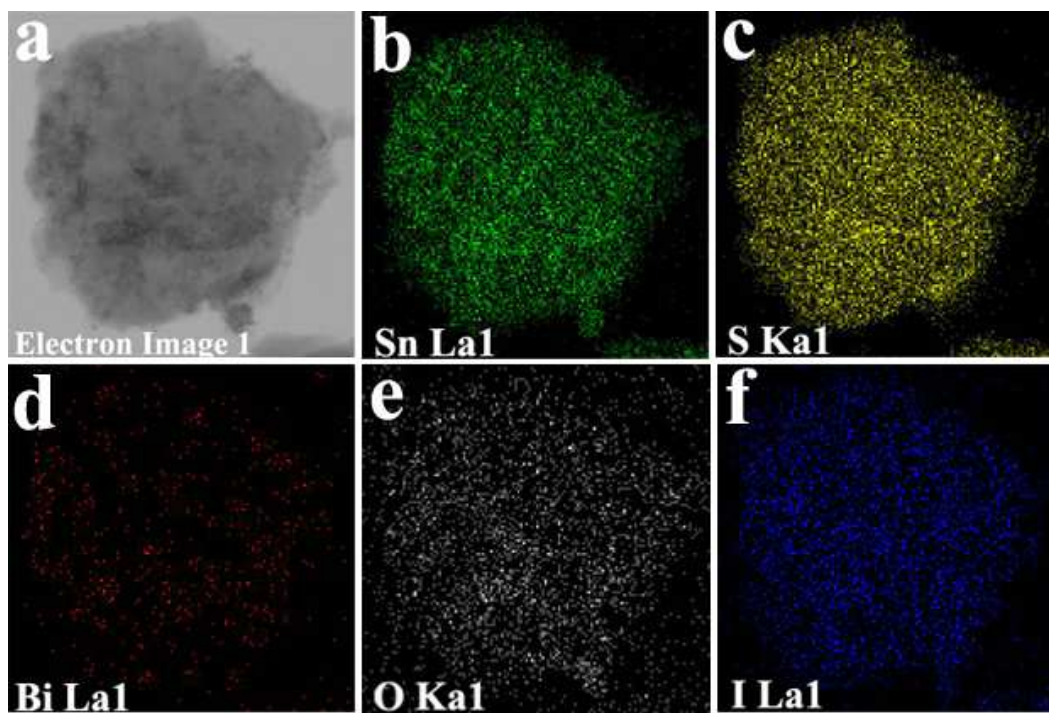


Fig. 4 EDS mapping of BiOI/SnS₂. The elements presented are (a), Sn (b), S (c), Bi (d), O (e), I (f).

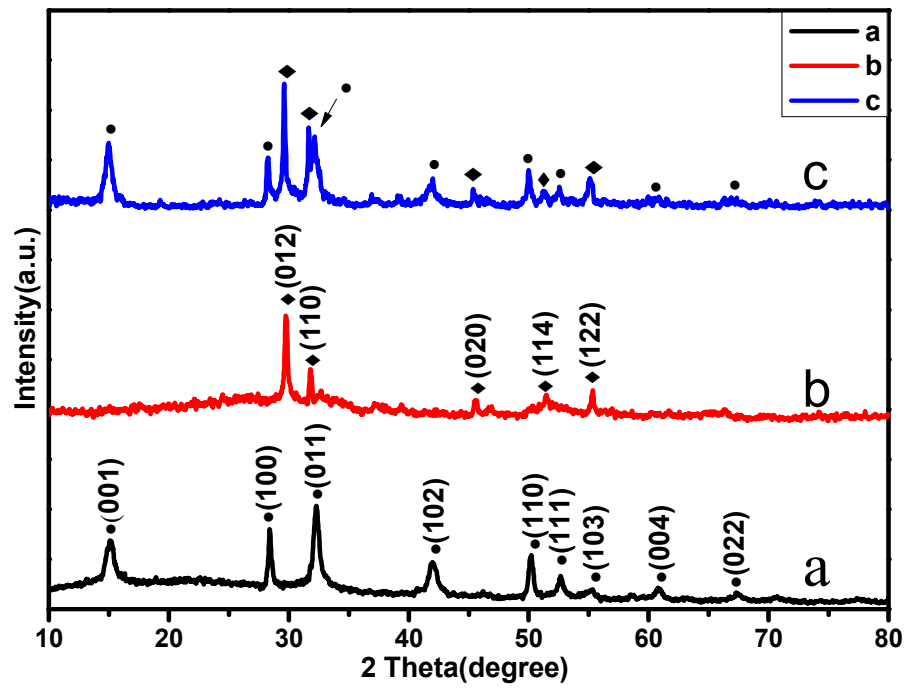


Fig. 5 XRD patterns of (a) pure SnS₂, (b) pure BiOI, (c) BiOI/SnS₂.

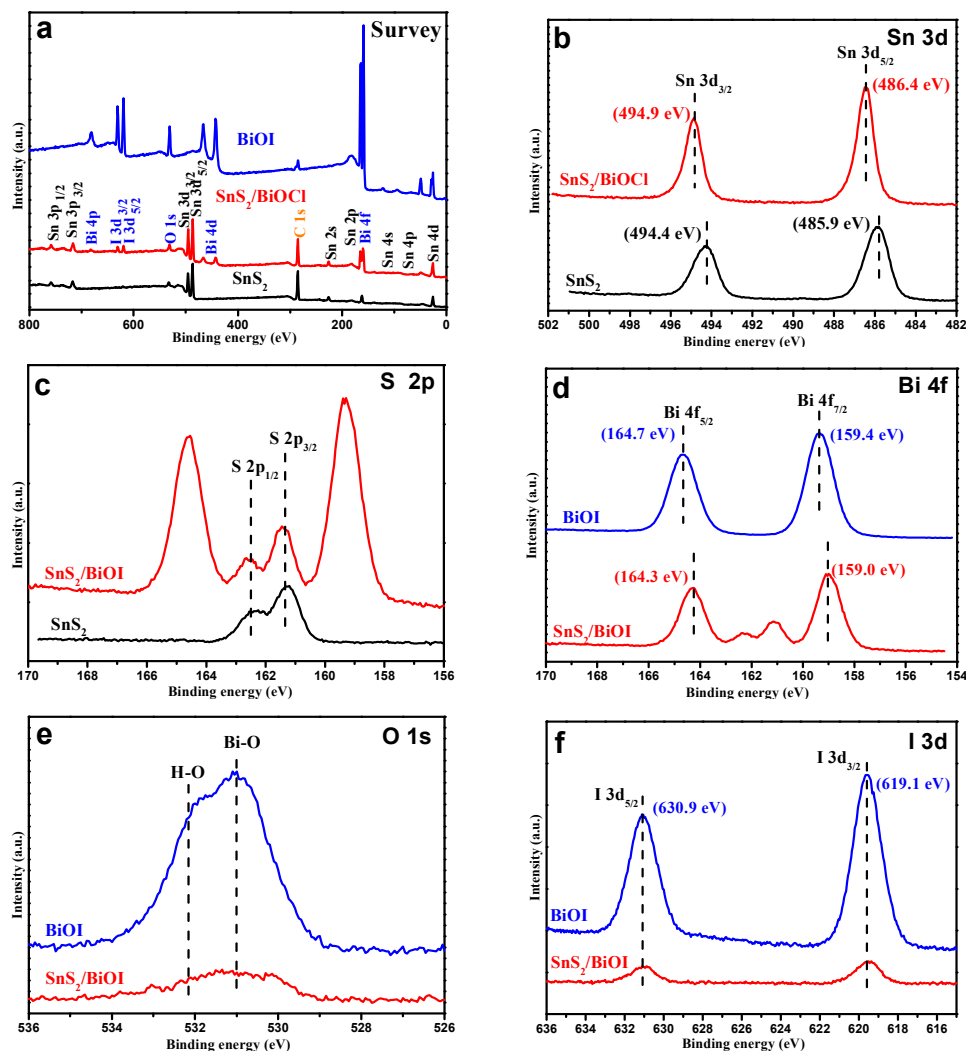


Fig. 6 XPS spectra of SnS₂, BiOI, and BiOI/SnS₂, survey spectrum (a), Sn 3d (b), S 2p (c), Bi 4f (d), O 1s (e), I 3d (f).

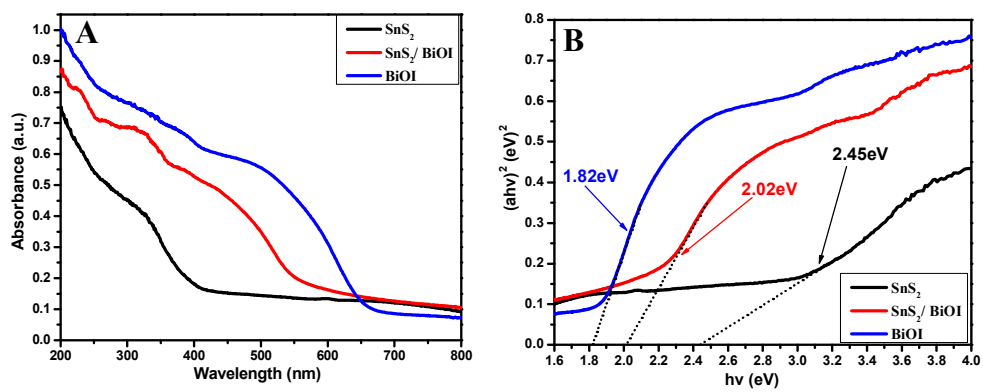
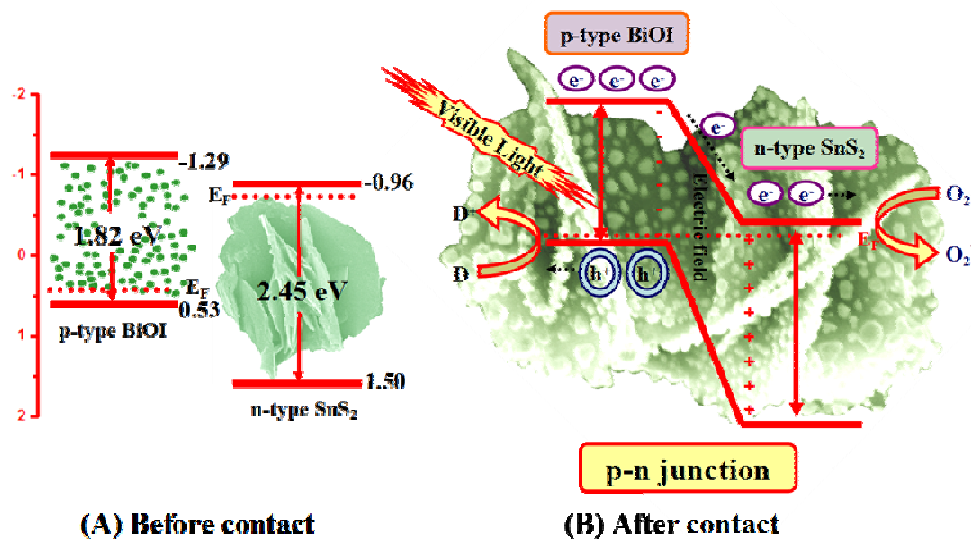


Fig. 7 UV-vis diffuse reflectance spectra (A) and (B) the plot of $(\alpha h\nu)^{1/2}$ vs band gap energy (hv) of pure SnS₂, pure BiOI, BiOI/SnS₂.



Scheme 1 Schematic diagrams for (A) energy bands of p-BiOI and n-SnS₂ before contact and (B) the formation of a p-n junction and its energy band diagram at equilibrium and transfer of photoinduced electrons from p-BiOI and n-SnS₂ under visible-light irradiation.

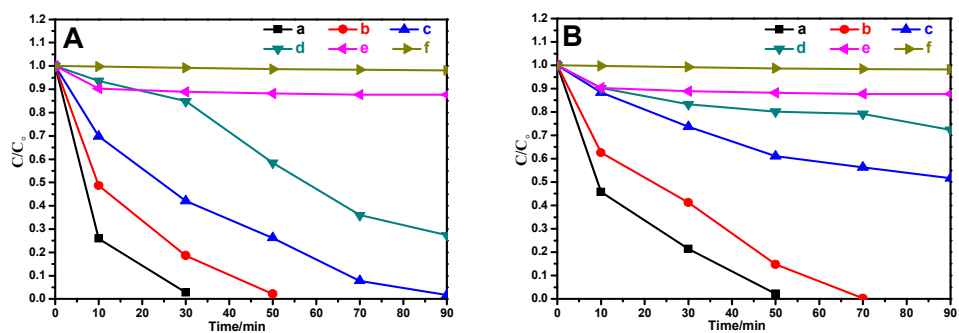


Fig. 8 Comparison of visible-light photocatalytic activities, (a) BiOI/SnS₂, (b) BiOI, (c) SnS₂, (d) P₂₅, (e) adsorption in dark, (f) degradation of 10 mg L⁻¹ RhB without photocatalyst under UV-vis (385-740 nm) (A) and visible light ($\lambda > 420$ nm) irradiations (B).

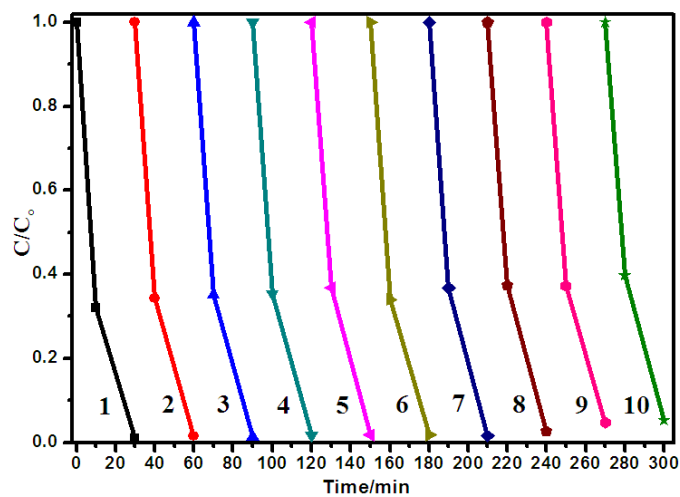


Fig. 9 Cycling degradation curves of BiOI/SnS₂ on the degradation of 10 mg L⁻¹ RhB under UV-visible light (385-740 nm) irradiations.

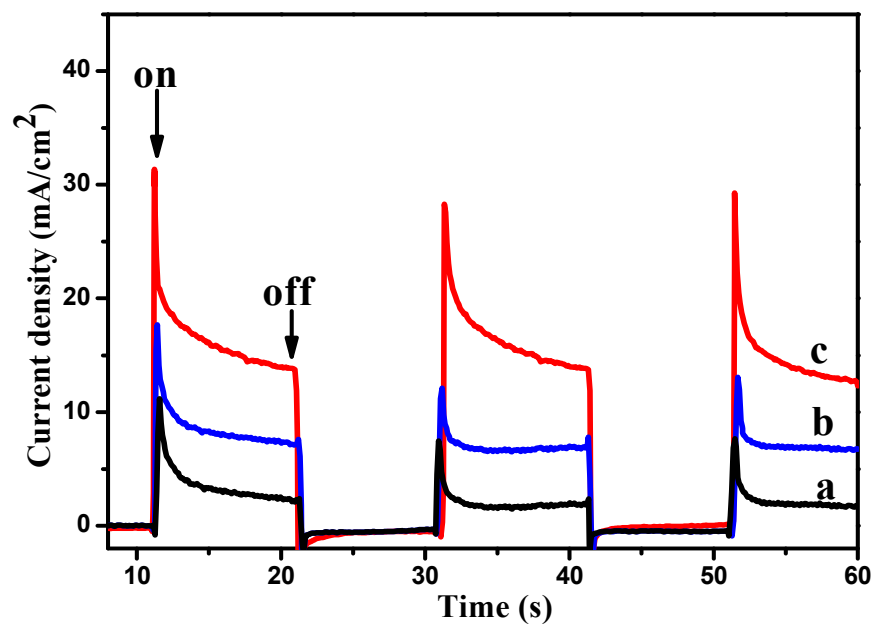


Fig.10 Comparison of transient photocurrent response of (a) pure SnS₂, (b) pure BiOI, (c) BiOI/SnS₂ in 0.1 M Na₂SO₄ aqueous solution under visible-light irradiation vs SCE.

Supporting information

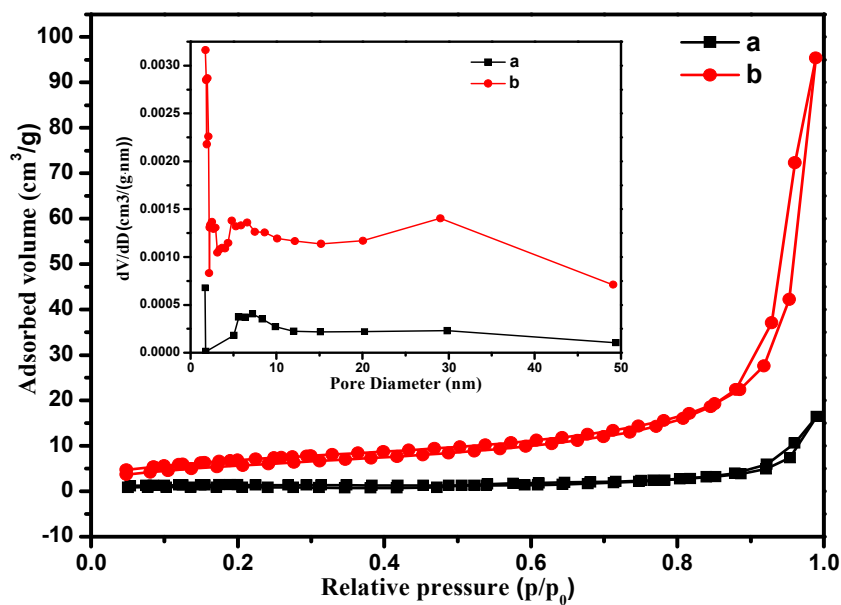


Fig. S1 Nitrogen adsorption isotherms and pore size distributions (insert) of (a) pure SnS₂ and (b) BiOI/SnS₂.

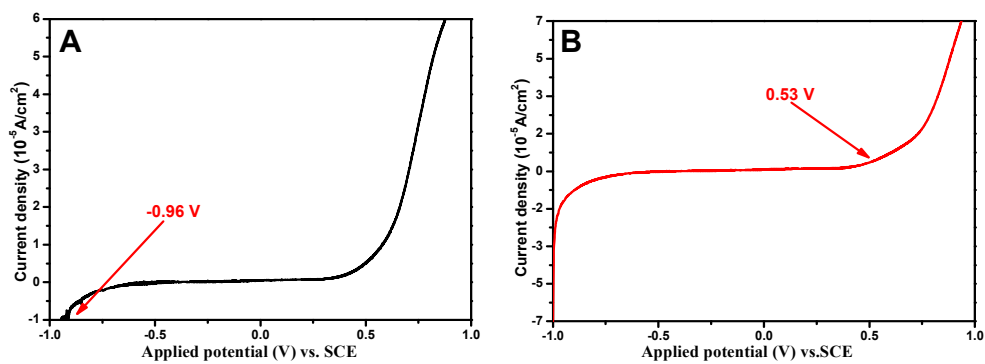


Fig. S2 Current-potential curves for (A) SnS₂ and (B) BiOI under Xe light irradiation ($\lambda > 420 \text{ nm}$).